TITLE

A heterogeneous drug tolerant persister state in BRAF-mutant melanoma is characterized by ion channel dysregulation and susceptibility to ferroptosis

AUTHORS

Corey E. Hayford[1], Philip E. Stauffer[1], Blake Baleami[1], B. Bishal Paudel[1,2], Darren R. Tyson[3], Aziz Al'Khafaji[4,5], Kaitlyn E. Johnson[5], Leonard A. Harris[6,7,8], Amy Brock[4,5], and Vito Quaranta[3,9]

[1]Chemical and Physical Biology Graduate Program, Vanderbilt University School of Medicine, Nashville, TN USA
[2]Department of Biomedical Engineering, University of Virginia, Charlottesville, VA USA
[3]Department of Biochemistry, Vanderbilt University School of Medicine, Nashville, TN USA
[4]Institute for Cellular and Molecular Biology, University of Texas at Austin, TX USA
[5]Department of Biomedical Engineering, University of Texas at Austin, TX USA
[6]Department of Biomedical Engineering, University of Arkansas, Fayetteville, AR USA
[7]Interdisciplinary Graduate Program in Cell and Molecular Biology, University of Arkansas, Fayetteville, AR USA
[8]Cancer Biology Program, Winthrop P. Rockefeller Cancer Institute, University of Arkansas for Medical Sciences, Little Rock, AR USA
[9]Department of Pharmacology, Vanderbilt University School of Medicine, Nashville, TN USA

ABSTRACT

There is increasing interest in cancer cell subpopulations that can withstanding treatment via non-genetic mechanisms, such as tumor cell plasticity and adaptation. These cell populations may be comprised of cells with diverse phenotypes, e.g., quiescent or slow cycling. Such populations have been broadly termed "drug-tolerant persisters" (DTPs) and may be responsible for minimal residual disease following anticancer treatment and acquired resistance. Understanding molecular mechanisms that drive emergence of DTPs could lead to new strategies to improve therapeutic outcomes. Recently, we reported that BRAF-mutant melanoma cells under prolonged BRAF inhibition enter a DTP state with balanced cell death and division, which we termed "idling." Here, we apply single cell barcoding to show that idling DTP populations emerge via cell state transitions, rather than selection of a few pre-existing drug-tolerant clones. Within the time frame of our experiments, DTPs exhibit varying proportions of fast- and slow-cycling cells within each lineage, suggesting that entry into the DTP state is a stochastic process. Furthermore, single-cell transcriptomics and bulk epigenomics reveal common gene expression and ontology signatures in DTP lineages that are consistent with rebalancing of ion channels. Calcium flux experiments uncover a reduction of divalent cation reserves in intracellular organelles, likely leading to endoplasmic reticulum stress. Accordingly, idling DTPs are more prone to ferroptotic cell death, as indicated by increased sensitivity to inhibition of glutathione peroxidase 4 (GPX4), which prevents removal of toxic lipid peroxides. In summary, we propose that ion channel homeostasis is a central process underlying idling DTP emergence in BRAF-mutated melanoma. Future studies will investigate translational aspects of this insight.

INTRODUCTION

Cancer is a complex and dynamic disease characterized by intratumoral cell-to-cell variability that has been implicated in treatment evasion and acquired resistance to therapy.[1,2] Tumor cells exhibit multiple forms of variability, due to a complex interplay between genetics, epigenetics, and other non-genetic sources of variation.[3] Historically, genetic variability has received the most attention, with pre-existing or acquired genetic resistance mutations implicated as the primary cause of treatment resistance and tumor relapse. However, recently, epigenetic factors have become increasingly recognized as major sources of tumor heterogeneity and consequent treatment failure.[4–6] Epigenetic heterogeneity, defined as co-existence of multiple distinct phenotypes within a population of genetically identical cells,[6] may result in long-term drug tolerance, from which new genetic resistance mutations can ultimately arise.[7,8] As such, it has been suggested that a window of opportunity might exist between the onset of drug tolerance and the acquisition of genetic resistance mutations during which a targeted secondary treatment can be deployed to further reduce, or even eliminate, the residual tumor mass.[7,8] Accomplishing this will require a detailed understanding of the molecular drivers underlying drug tolerance so that potential vulnerabilities can be identified and exploited clinically.

Multiple investigators have reported cancer cell subpopulations capable of withstanding drug treatments via non-genetic mechanisms. These populations have been broadly termed "drug-tolerant persisters" (DTPs) and described, variously, as either quiescent[9] or slow cycling.[10–12] Recently, we described a similar drug-tolerant state, termed "idling," that arises in BRAF-mutant melanoma cell populations under prolonged BRAF inhibition.[7,13] Importantly, in contrast to previously reported DTPs, the idling phenotype refers to the state of a cell population, rather than of individual cells. More precisely, we found that the growth dynamics of drug-treated BRAF-mutant melanoma cell populations were best described by a model in which cells are distributed across multiple phenotypic states, each with a distinct proliferation rate.[7] In the idling state, cells are proportionally distributed across these states, such that the proliferation rate of the population as a whole is approximately zero. Given the significant interest in drug tolerance as a precursor to treatment failure and acquired resistance in tumors,[14] recognizing that DTP populations may, in fact, be heterogenous, composed of multiple phenotypic states that act collectively to evade and survive drug treatment, is crucial for developing effective treatment strategies against them.

Here, we demonstrate experimentally in BRAF-mutant melanoma that the idling phenotype is a heterogeneous collection of phenotypic states, which is less heterogeneous than the collection of states in untreated populations. This reduction in heterogeneity under drug pressure suggests idling cells may potentially be vulnerable to a targeted secondary treatment. Single-cell RNA sequencing demonstrates that idling populations comprise multiple distinct transcriptomic states that are more similar to each other than the states observed in untreated populations. Furthermore, we use DNA barcoding to show that the idling state is populated by cells from most lineages present in the untreated population, suggesting that phenotypic state transitions, rather

than clonal selection, underlies the establishment of drug tolerance. A gene ontology (GO) analysis, combining data from both transcriptomics and epigenomics, indicates that ion channel expression is significantly altered in idling cells relative to untreated cells, pointing to a role for mitochondrial metabolism in the idling phenotype. This is supported by calcium flux assays that show store-operated calcium entry (SOCE) is significantly altered in idling cells. Finally, idling cell populations are shown to have increased susceptibility to death by ferroptosis, supporting the notion that DTPs are vulnerable to targeted secondary treatments.

RESULTS

Drug-tolerant melanoma populations include cells from almost all untreated lineages

We have previously shown that BRAF-mutant melanoma cell lines exhibit non-linear drug response dynamics to BRAF inhibitor (BRAFi). The initial phase of drug response is characterized by variable degrees of proliferation rate reduction. This is followed by entry of the treated cell population into a state of near-zero proliferation rate, termed idling.[7] To determine whether the idling state populations are comprised of a collection of DTP clones, we barcoded the BRAF-mutant SKMEL5 melanoma cell line with a gRNA barcoding library.[15] This approach allowed for high-depth coverage of dynamics for multiple lineages in response to selective pressures (i.e., drug treatment) and the ability to distinguish between clonal selection and phenotypic state transitions (FIG. 1A). Upon treatment with BRAFi PLX 4720 (8 μM for 8 days), the barcode library complexity was reduced by less than 10% (FIG. 1B). These surviving barcodes were shared in a large majority of replicates within each condition (untreated and idling; FIG. 1C), as well as between conditions (FIG. 1D). These results indicate that most clonal lineages survive treatment and persist at a similar relative proportion after BRAFi treatment. Simply, the idling state consists of cells from an overwhelming majority of the untreated population, providing direct evidence against clonal selection in response to BRAFi.

Some fluctuations in relative barcode abundance do exist after treatment with BRAFi (FIG. 1E, see next section). The underlying fold change distribution for the entire barcoded cell population from untreated to idling is a normal distribution centered at zero, with no obvious exceptions; the top 25 most populous barcodes reflect this distribution and are used for downstream analyses (FIG. 1F). Notably, nearly all the lineages that do not survive treatment come from clones that have an exceedingly small representation in the overall distribution, suggesting that the loss of those lineages is due to random chance. These results indicate that phenotypic state transitions likely dominate the response to BRAFi, leading a diverse set of clonal lineages to adopt a phenotypic state(s) akin to DTPs.

Melanoma populations become less transcriptomically heterogeneous following prolonged BRAF inhibition

We performed single-cell transcriptomics on the barcoded cell line in untreated and in idling conditions (see Methods). Using Uniform Manifold Approximation and Projection[16] (UMAP) to project the transcriptomic profiles for all cells into two dimensions, we see that untreated and

idling cells clearly fall in different regions of the UMAP space, with minimal overlap (FIG. 2A). Additionally, the idling cells reside in a more constrained region of the space, while in the untreated cells two distinct clusters are evident.

To quantify the variability within and between populations, pairwise distances were calculated between cells in each condition (FIG. 2B). Nearly all idling cells fall closer to one another than untreated cells fall to each other in the principal component analysis (PCA) space using 10 principal components. The Earth Mover's Distance (EMD) was calculated between the two pairwise distance distributions (EMD = 4.38) to measure the separation between the untreated and idling populations. In summary, the untreated population is more heterogeneous than the idling one in transcriptomic space.

Next, we aimed to determine the biological factors that differentiate the axes that separate population clusters. UMAP_2 (e.g., separation between untreated clusters) largely separates based on metabolic processes, consistent with our previous report of metabolic heterogeneity in untreated melanoma cells[7] (Supplementary FIG. S1A). Specifically, the large untreated (UT_L) cluster is enriched in a glycolysis gene signature compared to the small untreated (UT_S) cluster (see Methods, Supplementary FIG. S1D). Conversely, the idling population is enriched in an oxidative phosphorylation gene signature compared to both untreated clusters (Supplementary FIG. S1D). This is consistent with multiple reports in the literature, where BRAF-mutant cells rely primarily on glycolysis for growth and energy production, and BRAFi interferes with glycolytic processes, presumably favoring a switch to oxidative phosphorylation (see Discussion).

Alternatively, UMAP_1 primarily separates based on cell cycle stage, even after cell cycle gene signature regression, within the context of each cluster (Supplementary FIG. S1B). We used a previously established cell cycle gene signature (see Methods) to classify individual cells by cell cycle stage (G1, G2M, S). We then projected cell cycle stage on cells in the single-cell transcriptomics UMAP space (FIG. 2C). For visualization clarity, cell cycle stages were simplified into non-cycling (G1) and cycling (G2/M/S) states. The number and proportion of cells in cycling vs. non-cycling states were calculated (FIG. 2D), and the number of cycling cells is dramatically decreased in the treated population (67% vs 15%).

Changes in barcode abundance between untreated and drug-tolerant populations can be explained by simple random effects, not clonal selection

The barcoding system we adopted integrates droplet cell barcodes with transduced gRNA lineage barcodes, establishing a direct connection between the abundance of clonal lineages and their location in the single-cell transcriptomics state space. The barcoding library was designed with a relative low complexity (~65k potential barcodes, ~425 identified barcoded lineages), which allowed for multiple instances of the same lineage barcode in gene expression space. We projected the lineage distribution of SKMEL5 barcoded cells onto scRNA-seq UMAP space (examples in FIG. 3A). Barcodes exhibit various UMAP transcriptomic state occupancies and fall in both clusters (large and small) and cycling states across treatment conditions. In the untreated clusters, barcodes tend to have an approximately similar breakdown between small and large

clusters as the average of the population. However, in the idling cell cluster, the breakdown between non-cycling and cycling cell states tends to be predictive of clonal lineage drug response (FIG. 1E; FIG. 3B). From these examples, three key behaviors emerge. The first is exemplified by barcodes 5 and 9, where only a few cells (~5%) from the barcoded cell lineages fall in the cycling idling state region of the cluster. This low proportion of cycling cells potentially leads to a reduction in the relative proportion of these barcodes post-treatment (FIG. 1E-F). The second behavior, as seen in barcodes 2 and 13, is the opposite, where an increased proportion of cells in each barcode fall in the idling cycling state (~23%). This increase in cells in the cycling state potentially leads to an increase in the relative proportion of both lineages after treatment (FIG. 1E-F). The third is characteristic of most lineages and falls somewhere in between, which causes a middling effect on treatment response (Supplementary FIG. S2). Thus, a strong correlation (Pearson, R=0.55) exists between the proportion of cells in the cycling idling state and the relative fold change of barcode abundance after treatment (FIG. 3C), indicating that this is a shared feature of all barcoded cell lineages.

Multi-omics analysis points to ion channel dysregulation as a central factor in drug tolerance

Due to the time scale of the appearance of DTPs, it is generally accepted that DTPs may arise by epigenetic regulation rather than the accumulation of mutations.[9–12] To determine whether this is the case for transitions to the idling state, we performed bulk ATAC-seq on SKMEL5 cells before and after BRAFi treatment (see Methods). In each condition, we identified a fragment size distribution characteristic of a successful run (Supplementary FIG. S3B; library complexity in Supplementary FIG. S3A). Regions of open chromatin were enriched in cells from both conditions, resulting in unique and shared peaks between conditions (see Methods; FIG. 4A). These peaks were normalized to the transcription start site (TSS), and the distribution of binding loci (Supplementary FIG. S3C) was used to quantify the peak feature set (FIG. 4B). Idling peaks have much fewer proximal features (e.g., promoter regions) and more distal elements (e.g., distal intergenic and intronic regions) compared to the untreated condition. Distal elements have been known to be involved in short-term epigenetic regulation. Unique peaks were also assigned to a corresponding gene, and genes associated with unique peaks were input into a GO over-representation analysis, which identified ion transport and activity as differentiators of idling (FIG. 4C).

To confirm this finding independently, we subjected clonal sublines[7] of SKMEL5 (SC01, SC07, and SC10) to bulk RNA sequencing (RNA-seq) over the course of BRAFi treatment (0, 3, and 8 days post-BRAFi). Even though these sublines have marked short-term differences in terms of BRAFi response,[7] they were chosen because they all converge to a long-term near-zero proliferation rate characteristic of idling (3-8 days). To understand the time evolution of clonal subline response to BRAFi, normalized counts of each subline were projected into reduced dimensionality space by PCA (FIG. 4D).

On day 0, prior to BRAFi treatment, sublines are distinct on the first PCA axis (PC1), with SC07 and SC10 showing the most similarity. In short-term treatment (day 0 → 3), sublines predominately change on PC2 and maintain the overall variance between sublines observed at

day 0 (FIG. 4D). In the long-term response (day 3 → 8), the sublines begin to converge on both PC1 and PC2 (FIG. 4D). Considering that these three sublines are clonal derivatives of the SKMEL5 population, this result is consistent with the *en masse* transition of single cells to a common UMAP space after treatment (FIG. 3A).

A differential expression analysis was performed between untreated (day 0) and idling (day 8) across all three clones to identify transcriptomic signatures characteristic of idling. Differentially expressed genes were input into a GO over-enrichment analysis to reveal processes upregulated in the idling state. GO terms associated with ion transport and homeostasis were also found to be upregulated in idling cells (MF – FIG. 4E; BP – Supplementary FIG. S3D; CC – Supplementary FIG. S3E). In fact, statistically enriched GO terms shared a strong correlation between data modalities, with the most significant terms pointing to the ion channel activity shown in previous analyses (FIG. 4C and 4E). In summary, both epigenomics and transcriptomics data point toward ion channel activity as a major molecular determinant of the idling state.

Intracellular calcium ion flux is significantly reduced in drug-tolerant melanoma populations

Next, we experimentally tested calcium channel activity in idling versus untreated cells, using a calcium flux assay that measures the amount of ER resident calcium and propensity of SOCE activity. In this assay, cyclopiazonic acid (CPA) is used to inhibit the activity of Sarcoendoplasmic Reticulum Calcium ATPases (SERCAs), leading to a release of free calcium from the ER to the cytoplasm where it is detected by the calcium dye, Fluo-8-AM. (first peak, FIG. 5A). To replenish ER calcium upon depletion, cells undergo store operated calcium entry (SOCE) which brings in extracellular calcium that can then be pumped into the ER by SERCAs. In order to isolate ER calcium release from SOCE activity, CPA is added in a calcium free buffer, followed by addition of calcium to the assay (second peak, FIG. 5A). ER calcium release stimulates the opening of plasma membrane resident calcium channels (e.g., ORAI), but calcium cannot flow in until it is added to the assay buffer, allowing ER calcium content/release and propensity of SOCE activity to be studied separately. Idling cells exhibited decreased SOCE activity compared to untreated cells, demonstrated by the second peak (FIG. 5A). These results verify differences in ion channel activity in idling cells, and further suggest ER stress may be a vulnerability of idling cells.

To see if these differences in calcium flux may be a result of gene expression changes driven by BRAFi treatment, a differential gene expression analysis was conducted on bulk RNAseq data obtained from three SKMEL5 clonal sublines (FIG. 5B). Many of the queried calcium handling genes are differentially expressed in sublines after 3 days and 8 days of BRAF inhibition. Interestingly, trends in gene expression patterns seem relatively consistent across the sublines (FIG. 5B). These results show that calcium handling genes are differentially expressed in cell populations treated with BRAFi compared to untreated cell populations.

Drug-tolerant melanoma populations exhibit increased susceptibility to death via ferroptosis

Previous reports have indicated a connection between ion channels and ferroptosis, a type of regulated cell death, by way of increased ER stress.[17] Thus, induction of ferroptosis may provide a potential way to eradicate idling cancer cells. Indeed, expression of several genes in the ferroptosis signature is altered in melanoma cells upon BRAFi and entry into the idling state (FIG. 6A; Supplementary FIG. S4). Notably, glutathione metabolism gene expression is increased and genes for polyunsaturated fatty acid (PUFA) enzymes are decreased after BRAFi treatment, along with differences in various other parts of ferroptosis-related signaling. Interestingly, the expression pattern results in increased supply to the Fenton reaction, which produces the free radical precursors to reactive oxygen species (ROS), the step directly before commitment to ferroptosis (Supplementary FIG. S1E and S4).

To directly test susceptibility to ferroptosis, we subjected both drug-naïve and idling cells to treatment (see Methods) with RSL3; RSL3 is a compound that induces ferroptosis by targeting GPX4, a key regulator of glutathione oxidation and PUFA reduction. Interestingly, this treatment would reduce glutathione metabolism while preventing reduction of PUFA intermediates, leading to more precursors of the Fenton reaction and potentially to increased ROS that would drive cell death by ferroptosis. Interestingly, idling cells were ~3-fold more sensitive to RSL3 by potency (FIG. 6B; difference in IC50s), suggesting idling cells are susceptible to ferroptosis. Furthermore, addition of ferrostatin-1 (Fer-1), a drug that inhibits the production of lipid peroxides by the Fenton reaction (i.e., ROS), rescued the differential drug-response behavior of both idling and untreated cells in the presence of RSL3 (FIG. 6C). These results indicate that idling cells are vulnerable to ferroptosis, presumably due to the increased ROS that results from sequential GPX4 inhibition, providing a potential route to DTP elimination.

DISCUSSION

In this study, we show that BRAF inhibition (BRAFi) causes BRAF-mutant melanoma cells to transition *en masse* into idling populations of plastic drug-tolerant persisters (DTPs), which exhibit ion channel dysregulation and susceptibility to ferroptosis. Using cellular barcoding, we showed that idling cells result from an overwhelming majority of untreated clones, rather than clonal selection of a special idling clone (FIG. 1B-D). Distinct transcriptomic signatures were identified that differentiate untreated and idling cells, with the idling cells represented in a more restrained transcriptomic space (FIG. 2A-B). The idling cell population consisted of cells in cycling and non-cycling states, as defined by their phase in the cell cycle (FIG. 2C); though, the idling population had a lower proportion of cycling cells in its transcriptomic space than untreated cell populations (FIG. 2D). Barcoded clonal lineages were distributed across both transcriptomic states in the untreated condition (FIG. 3A). However, relative barcode abundances for lineages that have a larger proportion of cells in the cycling versus non-cycling idling state result in a larger proportion of that barcode in the idling population after treatment (FIG. 3A-C; c.f. FIG. 1E). Bulk epigenomics and time-series transcriptomics of the SKMEL5 cell line and clonal lineages identify a convergent idling molecular signature shared across modalities, which points towards ion dysregulation as a characteristic of the idling state (FIG. 4). The calcium ion channel dysregulation was validated in a calcium flux assay (FIG. 5A) and a differential gene expression analysis of ion channels (FIG. 5B). This evidence of calcium ion channel dysregulation further established a

potential connection to ferroptosis, a type of regulated cell death. A ferroptosis gene signature (FIG. 6A) suggested potential susceptibility to GPX4 inhibition through increased ROS; this susceptibility was validated to have a clear effect on idling cells (FIG. 6B). Rescue of the drugged phenotype by a lipid ROS scavenger verified the connection between idling drug tolerance and susceptibility to ferroptosis (FIG. 6C).

Many studies have remarked on the epigenetic plasticity as a way to understand decreased drug sensitivity,[18] and others have postulated using the epigenetic landscape as a mechanism to understand how cancer cells transition between states.[19] However, little experimental evidence exists showing how epigenetic state transitions lead to drug tolerance and eventual resistance. Together, these data provide evidence for a view of tumor cell plasticity where cells fall into basins across an epigenetic landscape. This study puts forth data that suggests a timeline for epigenetic plasticity of cancer cells prior to and after treatment. Tumor initiation from a single clone creates a population with the same genetic background. The genetic clone emanates an epigenetic landscape, comprised of several basins of attraction over which cells populate to create multiple cell types, each with different molecular phenotypes. Over time, cells in the landscape reach a dynamic equilibrium, i.e., cells can still transition between basins but the population is in a state of balance, a process known as "bet hedging".[20,21] The introduction of a perturbation, such as an anticancer drug treatment, upends the equilibrated landscape and drops cells into a new landscape. Cells re-equilibrate to the new landscape and adopt cell fates corresponding to the state in which they now reside. In the case of a drug with good efficacy, most cells will fall into a state of the drug-treated landscape that results in death. However, if the new landscape includes a state where cells have a positive proliferation rate in drug, the population will invariably rebound. In our case, most of the cells matriculate into the large non-cycling state upon treatment with BRAFi, but some end up in a smaller cycling state (FIG. 2C). This feature is consistent with several different types of DTPs, from quiescent to slow-cycling.[9–12] However, some barcoded clonal lineages disproportionally fall into one of the two states (FIG. 3A), leading to a differential short-term drug fitness in response to BRAFi. Previous studies in the lab show that even sublines eventually adopt a near-zero proliferation rate in prolonged BRAFi,[7] suggesting that lineages fully equilibrate to the new landscape over time. This occurrence is largely consistent with other oncogene-addicted cancers treated with targeted therapies, which exhibit a noisy short-term drug tolerance that often leads to long-term genetic resistance.[22,23]

An actionable result of a drug-modified landscape is new biochemical network properties that can lead to new treatment sensitivities. This phenomenon, in which resistance (or tolerance) to one drug treatment confers sensitivity to a different drug (or drug class), is commonly known as "collateral sensitivity." Interesting screens have been performed to identify drugs that have increased sensitivity for cells treated with an initial drug, including in cancer.[24] However, these methods ignore the heterogeneity present in treated populations and often lead to traditional up-front combination therapies. These combination therapies create an entirely new epigenetic landscape that has new molecular properties with unknown vulnerabilities,[6,25] making the new tumor difficult to treat. The heterogeneity identified in our idling cells exemplifies this problem and, therefore, requires a different approach. Sequential therapy is an alternative approach in which cells are able to equilibrate to the new drug-treated landscape with the hope that it is

more sensitive as a whole.[26] Molecular analyses in our study show that the drug-treated landscape is indeed more homogeneous (FIG. 2A) and has a common thread in ion channel activity across transcriptomics and epigenomics data (FIG. 4). By targeting the idling state with a sequential therapy that leverages the increased ion channel activity to promote targeted ferroptotic cell death, we seemingly create another epigenetic landscape where all of the basins have a negative proliferation rate in drug treatment and result in tumor eradication. Therefore, potential future studies could be aimed at identifying vulnerabilities of epigenetic landscapes that result after primary drug treatment and finding patient-specific secondary drugs used for sequential drug treatment regimens that eradicate the entire tumor. Together, these results indicate that BRAF-mutant melanoma cells converge to a confined idling population after BRAFi treatment, yet still exhibits cycling and non-cycling transcriptomic states. This breakdown appears to encapsulate previously described DTPs that exhibit various cycling behaviors, including quiescence, active division, and slow cycling.

Figure captions

Figure 1: ***Most clonal lineages survive treatment with BRAFi into idling.*** (A) Schematic of example lineage tracing experiments using cellular barcoding. (B) Number of unique barcodes in each treatment condition. Lines correspond to the means of three experimental replicates (points). A minimum cutoff of 100 counts per million (CPM) was used. (C) Proportional sharing of barcodes among experimental replicates (i.e., R1 = replicate 1) for each treatment condition. (D) Heatmap of relative barcode abundances ($\log_{10}$ CPM) for each experimental replicates across all captured barcodes. Heatmap is organized by decreasing barcode abundance in untreated condition. (E) Relative fraction of the top 25 ranked (in untreated) barcoded cell lineages in untreated and idling conditions. Bar height corresponds to the average of three experimental replicates (line is standard deviation). (F) Distribution of ($\log_2$) fold change for barcoded clonal lineages from untreated to idling. Means of fold changes were compiled into a distribution for all captured lineages (grey), as well as the top 25 most abundant lineages noted in *E*.

Figure 2: ***Idling cells represent a convergent, yet still heterogeneous, transcriptomic state with less idling cells in the cycling state than untreated cells.*** (A) UMAP projection of untreated and idling single-cell transcriptomes. 6410 cells are shown, with an approximately equal split between conditions. (B) CDF of pairwise cell distances (random sampling of 15,000) with 10 principal components on the PCA space of the untreated and idling single-cell transcriptomic data. An Earth Mover's Distance (EMD) was calculated between the distributions to quantify their separation from each other. (C) Overlay of cell cycle state (see Methods) on UMAP projection of single cell transcriptomes (colored contours represent information in *A*)**.** (D) Relative proportion of cells in cell cycle state for major untreated and idling clusters. The total number of cells in each cluster (n) is noted above each bar.

Figure 3: ***Lineage distribution across cell cycle states is reflective of clonal dynamics.*** (A) Projections of lineage transcriptomic distributions on UMAP projection in *FIG. 2A*. Lineages correspond to colored dots, while contours reflect treatment condition. (B) Proportion of cells in the idling cycling transcriptomic state for the top 25 most abundant barcodes. Dashed line

represents average of all barcodes. (C) A Pearson correlation analysis was performed between the percentage of cycling cells in the idling state and the $\log_2$ fold change in barcode abundance following BRAFi treatment for the top 25 most abundant barcodes.

Figure 4: ***Unique elements of the idling transcriptome and epigenome have differential features for ion activity.*** (A) Venn diagram of ATAC-seq identified peaks of open chromatin. (B) Alignment of peaks to the TSS allows for prediction of epigenomic features.-Predicted feature distribution in untreated, idling, or shared peaks. Peaks were assigned to features based on proximity to TSS (see Methods). (C) GO over-enrichment analysis of genes associated to unique idling peaks. The top 10 terms with the largest gene ratio are shown. (D) PCA projection of subclones (SC01, SC07, and SC10) at multiple times (0, 3, and 8 days) in BRAFi. Each condition (e.g. SC01 at day 0) was completed in triplicate. Lines are drawn between the centroids of triplicates across the time series. (E) GO over-representation analysis on differentially expressed genes with increased expression between untreated and idling. GO terms with the top 10 largest gene ratios (see Methods) are shown.

Figure 5: ***Idling cells have decreased calcium flux and altered expression of calcium handling genes.*** (A) Calcium flux assay of untreated and idling cells using cyclopiazonic acid (CPA) to deplete ER calcium without extracellular Ca^{2+}, addition of extracellular Ca^{2+} to test store operated calcium entry (SOCE) activity, and ionomycin to control for number of cells in the assay. (B) Differential gene expression analysis of calcium handling genes in sublines transcriptomics data from *4D*.

Figure 6: ***Idling cell populations are susceptible to ferroptosis.*** (A) Gene expression values (z-scores; see Methods) for multiple clonal sublines (SC01, SC07, SC10) across the BRAFi treatment time course (0, 3, and 8 days post treatment). Genes are further grouped by their associated processes related to ferroptosis. (B) DIP rate dose response curves for untreated and idling cells treated with ferroptosis inducer RSL3. (C) Same as *B,* except with rescue experiments on the post-treated cells using ferroptosis inhibitor Fer-1.

Figure S1: ***Analysis of the UMAP single cell transcriptomic space.*** (A) GO analysis of differentially expressed between the untreated clusters in the UMAP single cell transcriptomics space shown in *FIG. 2A.* (B) Same as *A* except the analysis was applied to the idling cluster and a subpopulation of cells that were predominantly in the cycling state. (C) A representation of UMAP single cell transcriptomic space of untreated and idling cells used for differential gene expression and GO analyses in *D* and *E*. (D) Distributions of the signature scores for cells in each cluster in the differential gene expression analysis from the GO analysis related to glycolysis and oxidative phosphorylation. Colors of each distribution correspond to the colors of the clusters in *C*, where pink is cluster 1 (i.e., UT_S), yellow is cluster 2 (i.e., UT_L), and blue is cluster 3 (i.e., idling). (E) Same as *D* except with other processes.

Figure S2: ***Lineage distributions for barcodes with a middle effect in clonal dynamics to treatment response.*** Same as *FIG. 3A* for the remaining top 25 barcodes in the single cell transcriptomics analysis.

Figure S3: ***Quality control of bulk epigenomics ATA-seq data and correlation analysis of differentially expressed genes in idling transcriptome and epigenome.*** (A) Plot of unique reads versus sequenced reads for the bulk ATAC-seq data used in epigenome analyses. (B) Insert size distribution of aligned reads from ATAC-seq data on untreated and idling cells. Both conditions follow traditional nucleosome patterning. (C) Peak binding site distribution for untreated, idling, and shared peaks. X-axis represents kb distances from the TSS. (D) Correlation analysis of the differentially expressed genes from a Biological Process (BP)-type of GO analysis for the epigenome and transcriptome of the idling cell population. (E) Same as *D* for a Cellular Component (CC)-type of GO analysis.

Figure S4: ***Ferroptosis pathway*****.** A schematic diagram of the ferroptosis pathway with boxes that correspond to the colors of the groups for the genes in *FIG. 6A*.

MATERIALS AND METHODS

Cell culture and reagents

We chose BRAF-mutant melanoma cell line SKMEL5 as a preferred model, since it exhibits median BRAFi sensitivity compared to other BRAF-mutant melanoma cell lines.[27] SKMEL5 cell line was purchased from ATCC© and labeled with either a fluorescent histone H2B conjugated to the monomeric red fluorescent protein (H2BmRFP) and a cellular barcoding library (see "Cellular barcoding" below) or H2B conjugated to the green fluorescent protein (H2B-GFP). Single cell-derived subclones of SKMEL5 were selected and derived by limiting dilution, as described previously. Cells were cultured in a mixed media of DMEM and Ham F-12 media (DMEM:F12 1:1; catalog no. 11330-032), supplemented with 10% fetal bovine serum (FBS). Cells were incubated at 37°C, 5% CO_2, and passaged twice a week using TrpLE (Gibco). Cell lines and sublines were tested for mycoplasma contamination using the MycoAlert™ mycoplasma detection kit (Lonza), according to manufacturer's instructions, and confirmed to be mycoplasma-free. BRAF inhibitor PLX 4720 (analog to Vemurafenib), ferroptosis inducer RSL3 and ferroptosis inhibitor Fer-1 were obtained from MedChem Express (Monmouth Junction, NJ) and solubilized in dimethyl sulfoxide (DMSO) at a stock concentration of 10mM and stored at -20°C. Cell lines were originally stored at -80°C, then moved into liquid nitrogen.

Cellular barcoding

Setup: Cellular barcoding library was constructed by cloning a guide RNA (gRNA) library of barcodes into a CROP-seq-BFP-TSO vector as previously described. The vector was engineered such that barcodes can be isolated by isolation and amplification (barcode sampling) or mRNA capture in a single-cell RNA sequencing (scRNA-seq) experiment. gRNAs were built as a 20-nucleotide sequence of four nucleotides identical among all barcodes, followed by a 16 strong-weak (SW) paired nucleotides (i.e., XXXXSWSWSWSWSWSWSW). The SW pairing of the barcode sequence was designed to prevent polymerase chain reaction (PCR) amplification bias.

The maximum complexity of this library is 2^{16} (~65,000 unique barcodes). The barcode library vector was used to produce lentiviral libraries using a lipofectamine transfection of HEK293T cells. Media containing lentiviral particles were collected at 48- and 72-hours post-transfection, pooled, filtered through a 0.45 um Nalgene syringe filter and concentrated using a 50 mL size-exclusion column by centrifugation at 2200 RCF at 4°C for two hours. Concentrated virus was stored in -80°C. SKMEL5 cells were seeded in a 6-well plate at ~$1x10^6$ cells per well in 2.5 mL culture media. Cells were transduced with the barcoded CROP-seq-BFP-TSO-Barcode_sgRNA lentivirus using 0.8 μg/mL in each well and a multiplicity of infection (MOI) of 0.05. Twenty-four hours after incubation, transduction media (containing polybrene) was exchanged for fresh culture media. Forty-eight hours after incubation, barcoded cells were isolated by fluorescence-activated cell sorting (FACS) and subsequently cultured until confluence in a T-150 dish and then cryopreserved. Cryopreserved cells were thawed in a T-25 dish and scaled up for ~2 weeks in two separate sets. The first set of thawed cells were treated with 8uM PLX4720 (and an untreated control) for eight days and subjected to barcode sampling (see "Barcode Sampling Analysis" subsection below). The second set was plated in three T-75 flasks (parallel replicates) and independently treated with 8μM PLX4720 (or untreated control) for eight days and subjected to scRNA-seq by the 10X genomics Chromium platform (version 2 chemistry; see "RNA single-cell transcriptome sequencing" section below for more details). In both cases, treated cells had media and drug replaced every three days. Untreated cells were expanded completely over the course of the time course (i.e., no cell splitting).

Barcode Sampling: After PLX4720 treatment for eight days (or no treatment expansion), cells in the first set were pelleted for genomic DNA (gDNA) extraction using the DNeasy Blood and Tissue Kit (Qiagen) per manufacturers' instructions. Barcode sequences were amplified for each replicate by polymerase chain reaction (PCR; 98°C for 30 seconds, followed by 22 cycles of denaturation - 98°C for 10 seconds, annealing - 63°C for 30 seconds, extension - 72°C for 10 seconds, and a final extension of 72°C for 5 minutes) using primers containing flanking regions and Illumina adapter index sequences. 2ug gDNA was used in each PCR reaction, and a combination of 5 distinct pooled forward primers were utilized to minimize sequencing error. Reactions were purified using a 1.8x AMPure XP bead (Beckman Coulter) cleanup. Reaction products were confirmed using agarose gel confirmation (band at ~215bp). The resulting libraries were quantified using a Qubit fluorometer (ThermoFisher), Bioanalyzer 2100 (Agilent) for library profile assessment, and qPCR (Kapa Biosciences Cat: KK4622) to validate ligated material, according to the manufacturer's instructions. The libraries were sequenced using the NovaSeq 6000 with 150 bp paired end reads as sequencing spike-ins (targeting ~200k reads). RTA (version 2.4.11; Illumina) was used for base calling and MultiQC (version 1.7) for quality control.

Barcode Sampling Analysis: Barcodes were identified from amplified sequence reads by trimming flanking adapter sequences. Barcodes abundances were totaled and normalized to library read depth, resulting in reads per million (RPM). Barcodes less than 100 CPM were removed from the analysis. Numbers of unique barcodes were calculated based on this threshold. Overlaps between experimental replicates were calculated to determine the proportion of barcodes shared across different runs. Total barcode abundance (including low abundance barcodes) was

calculated using the $\log_{10}$ of barcode RPM for each replicate. Relative barcode fraction was calculated for each sample across three replicates. Log_2 fold change of the idling to untreated mean barcode fractions was calculated for all barcodes above the CPM threshold.

RNA single-cell transcriptome sequencing

Data Collection: After PLX4720 treatment for eight days (or no treatment expansion), cells in the second set were prepared targeting ~3000 cells per sample, washed, and resuspended in 0.04% bovine serum albumin (BSA) in phosphate-buffered saline (PBS). Cell suspensions were subjected to 10X Genomics single-cell gene expression protocol (version 2, 3' counting) in two separate wells, according to manufacturer's guidelines. Single-cell mRNA expression libraries were prepared according to manufacturer instructions. Due to the nature of gRNA barcoding library construction, mRNAs resulting from gRNA barcodes were captured along with other mRNAs. Libraries were cleaned using SPRI beads (Beckman Coulter) and quantified using a Bioanalyzer 2100 (Agilent). The libraries were sequenced using the NovaSeq 6000 with 150 bp paired-end reads targeting 50M reads per sample for the mRNA library (including barcode library). RTA (version 2.4.11; Illumina) was used for base calling and MultiQC (version 1.7) for quality control. Gene counting, including alignment, filtering, barcode counting, and unique molecular identifier (UMI) counting was performed on each library using the *count* function in the 10X Genomics software *Cell Ranger* (version 3.0.2) with the GRCh38 (hg38) reference transcriptome.

Transcriptome Analysis: Cell Ranger output two single-cell gene expression matrices, for untreated and idling cells. scUniFrac was performed to quantify the degree of overlap between conditions. Finding minimal overlaps, and since cells were prepared and processed in parallel, no computational batch correction was performed. Seurat was used to perform gene expression analysis. The *SCTransform* function was used to regress out mitochondrial gene expression (percent.mt), number of features (genes; nFeature_RNA), number of RNA molecules in the cell (nCount_RNA), and cell cycle variables (S.Score and G2M.Score). Feature selection was performed according to Seurat guidelines using a variance stabilizing transformation of the top 2000 most variable features. Data was normalized and scaled according to Seurat guidelines. Data between conditions were combined and visualized using the Uniform Manifold Approximation and Projection (UMAP) dimensionality reduction algorithm as implemented in Seurat. In addition to UMAP, t-distributed Stochastic Neighbor Embedding (t-SNE) and Principal Component Analysis (PCA) were also performed, using the Seurat implementation. Clustering was performed in the joint UMAP space using the default Seurat implementation, a shared nearest neighbor (SNN) modularity optimization-based method. Pairwise Euclidean distances were calculated between cells in each condition with 10 principal components in the PCA space and plotted as a cumulative density function (CDF). An Earth Mover's Distance (EMD) was calculated between 15000 randomly sampled pairwise distances using the *wasserstein1d* function in the *transport* R package. Differential expression analysis was performed between conditions (untreated, idling), between combined clusters (large, small) within each condition, and between clusters across conditions (e.g., $\text{untreated}_{\text{large}}$ vs. $\text{idling}_{\text{large}}$). Differential expression was performed using the Seurat *FindMarkers* function and DEGs (adjusted-$p < 0.05$) were input into a GO over-enrichment analysis. The GO analysis identified cell cycle as a major factor

separating idling clusters and was not present for untreated clusters. Therefore, using cell cycle scores, a cell cycle phase (G1, G2M, S) was assigned to each cell, which was further simplified into cycling (S, G2M) and non-cycling (G1), which we call cell cycle state. Cluster proportion was calculated by cell cycle state to quantify the differences between clusters. The number of cells in each cell cycle state were tallied and calculated as a percentage across each cluster.

Barcode Analysis: After calculation of scRNA-seq gene expression matrices, barcode abundances were incorporated to the matrices. To do this, gRNA lineage barcodes had to be mapped to their associated 10X cell barcodes. First, unmapped scRNA-seq BAM files were cleaned to only include the mRNA transcript ID, scRNA-seq cell barcode, and scRNA-seq unique molecular identifier (UMI). Mapped scRNA-seq BAM files (3' heavy) were cleaned to only include the mRNA transcript ID and lineage barcode (from gRNA library). Unmapped and mapped subsets were merged on the mRNA transcript ID to assign a lineage barcode to each cell barcode and UMI. The resulting merged dataset was paired down to a single cell barcode – lineage barcode pair, which was appended to each cell in the gene expression matrix as a metadata tag. Barcode abundances were totaled across all cells in the experiment that captured a barcode, and strongly reflected barcode sampling relative abundances and fold changes upon treatment (FIG. 1E - scRNA-seq barcode fractions). Barcodes were overlaid on UMAP projections of scRNA-seq data, and further categorized into the cycling and non-cycling transcriptomic states (see Transcriptome Analysis subsection). Total number of cells from each barcode were tallied across each transcriptomic cell cycle state, and a percentage (relative to each barcode) in each state was calculated. A correlation analysis (Pearson) was performed on the percentage of cycling cells in idling vs. the $\log_2$ barcode fold change after treatment.

Functional interpretation analysis: The single-cell transcriptome count matrix (see "RNA single-cell transcriptome sequencing:Data Collection" above) was scaled by multiplying counts by the median RNA molecules across all cells and dividing that number by the number of RNA molecules in each cell (as recommended). Gene signature files were obtained from the molecular signatures database (MSigDB). *Hallmark* gene sets (50 in total) were downloaded from MSigDB (gsea-msigdb.org/gsea/msigdb/genesets.jsp?collection=H). Both the scaled counts matrix and each of the hallmark gene sets were input into VISION[28] to identify gene signature scores for each cell-signature pair. Four hallmark gene sets (KRAS_SIGNALING_UP, KRAS_SIGNALING_DOWN, UV_RESPONSE_UP, UV_RESPONSE_DOWN) were condensed into two (KRAS_SIGNALING, UV_RESPONSE) by VISION to leave 48 total gene signatures. Scores were compiled into a distribution and plotted by cluster (k=3) for each gene set.

Bulk RNA transcriptome sequencing

Data acquisition: Total RNA was isolated from untreated SKMEL5 single cell-derived subclones, each in triplicate, using Trizol isolation method (Invitrogen), according to the manufacturer's instructions. RNA samples were submitted to Vanderbilt VANTAGE Core services for quality check, where mRNA enrichment and cDNA library preparation were done with Illumina Tru-Seq stranded mRNA sample prep kit. Sequencing was done at Paired-End 75 bp on the Illumina HiSeq

3000. Reads were aligned to the GRCh38 human reference genome using 'HISAT2' and gene counts were obtained using 'featureCounts'.

Data analysis: RNA-seq data was analyzed using the DESeq2[29] R package. Cells with less than 18 reads per condition were removed, according to DESeq2 vignettes. Counts were transformed using the regularized logarithm (rlog) normalization algorithm. PCA was performed using the *prcomp* function in R. The path between time series data points was visualized as a line between subline-time point replicate means in the PCA space. EMDs were calculated between pairwise distance distributions for each subline across the treatment time series and for each time point across the sublines. Hierarchical clustering was performed using the *hclust* R function with a Ward's minimum variance method. Differential expression analysis was performed using a model design to quantify both changing variables and their interaction (~ subline + treatment time + subline:treatment time). DEGs across sublines between untreated (pre-treatment, day 0) and idling (day 8 post-treatment) were identified (adjusted-$p < 0.05$, log2 fold change > 2). DEGs were input into a GO enrichment analysis, which identified GO terms associated with "Biological Process" (BP), "Molecular Function" (MF), and "Cellular Component" (CC) GO types.

Ferroptosis gene signature analysis: A ferroptosis gene signature was obtained from the Kyoto Encyclopedia of Genes and Genomes (KEGG). For each subline, genes were normalized to the 0-day time point and a $\log_2$ fold change was calculated compared to the 0-day baseline. Groupings of genes were annotated by separate signaling processes (Supplementary FIG. S5).

Bulk ATAC epigenome sequencing

Data acquisition: Data was collected using the omni-ATAC protocol for bulk ATAC sequencing (ATAC-seq). After PLX4720 treatment for eight days (or no treatment expansion), cells in the second set (in parallel to barcode sampling data collection) were pelleted at 50k cells and resuspended in a cold ATAC-seq resuspension and lysis buffer containing NP40 (0.1%), Tween20 (0.1%), and Digitonin (0.01%) and incubated on ice. A resuspension buffer was added (0.1% Tween20, no NP40 or Digitonin) to wash out the lysis reaction. Cells were pelleted and resuspended in a transposition mix (5x Tris-DMF, PBS, 1% digitonin, 10% Tween20, nuclease-free H_2O), including transposase Tn5, followed by a 30-minute incubation at 37°C, with shaking to enhance tagmentation. After 30 minutes, the reaction was stopped by adding a DNA binding buffer (Zymo) and purified using a DNA Clean and Concentrate kit (D4004, Zymo). The final product was eluted in nuclease-free H_2O. PCR amplification was performed on the eluate with an NEBNext 2X High Fidelity PCR Mix (NEB, M0541S) N7, and N5 index sequencing primers (extension at 72°C for 5 minutes; denaturation at 90°C for 30 seconds; 12 cycles: denaturation at 98°C for 10 seconds, annealing at 62°C for 30 seconds, extension at 72°C for 30 seconds; final extension at 72°C for 5 minutes). The PCR product was purified with the Zymo DNA Clean and Concentrate kit and eluted in 22µL nuclease-free H_2O. ATAC-seq PCR libraries were visualized by agarose gel electrophoresis for a quick check for the nucleosome ladder pattern (bands over ~150 bp). Libraries were also quantified using a Qubit fluorometer (ThermoFisher), Bioanalyzer 2100 (Agilent) for library profile assessment, and qPCR (Kapa Biosciences Cat: KK4622) to validate

ligated material, according to the manufacturer's instructions. The libraries were sequenced using the NovaSeq 6000 with 150 bp paired-end reads as spike-ins on the sequencing chip (untreated: ~160m, idling: ~130m reads). RTA (version 2.4.11; Illumina) was used for base calling and MultiQC (version 1.7) for quality control.

Data Analysis: Reads were trimmed using *cutadapt* (paired-end) to remove primer sequences and aligned to the hg38 reference genome using the *bwa mem* function in Burrows-Wheeler Aligner (BWA, version 0.7.17). Aligned reads were sorted and duplicates were marked using Picard (version 2.17.10). Untreated reads had more detected duplicates (~78% compared to ~32% in idling). Reads were deduplicated, but to address the discrepancy in deduplicated library complexity, idling reads were subsampled (25% of original library, Supplementary FIG. S4A-B) to achieve a similar complexity to the untreated. Reads were further cleaned according to sequence quality guidelines. Insert sizes were plotted from the output of *InsertSizeMetrics* after deduplication in Picard. Peaks of open chromatin were called using the *MACS2 callpeak* function according to recommended guidelines for ATAC-seq data (BAM paired-end method, q-threshold: 0.05, no MACS2 model, shift: -100, extension size: 200). Peaks were subjected to a further round of quality control and cleaning using *ChIPQC* (peak mapping, peak duplication, blacklist peak detection), and blacklisted peaks were removed. Peaks were converted to consensus counts using the *runConsensusCounts* function in *soGGi*. Intersections of and unique cleaned peaks were determined and visualized as a Venn diagram using the *vennDiagram* function in the *limma* package. Unique and intersection peaks were annotated with the nearest neighbor genes using the *annotatePeak* function and hg38 transcriptome in the *ChIPseeker* package. These peaks were also re-aligned to the transcription start site (TSS) for each gene. Average profiles of read subsets across all genes (nucleosome-free, mono-nucleosome, and di-nucleosome; normalized to the TSS). Peaks were classified based on closeness to the TSS and assigned to predicted feature (promoter, UTR, exon, intron, downstream, distal intergenic). Genes associated with unique and intersections of peaks were input into a GO enrichment analysis for BP, MF, and CC GO types (same as "Bulk Transcriptome Analysis" above). Transcription factor (TF) footprinting in the region around TSSs was performed on untreated and idling unique peaks for key TFs.

Gene ontology analysis

Setup: Genes associated with unique ATAC-seq peaks (see "Bulk ATAC Epigenome Sequencing: Data Analysis" above) were identified for each condition (i.e., untreated or idling). Additionally, DEGs from the bulk RNA-seq statistical analysis were determined (8-day vs. 0-day time points across all clonal sublines; see "Bulk RNA Transcriptome Sequencing:Data Analysis" above). The two gene lists were independently subjected to a GO enrichment analysis using '*clusterProfiler*'. Genes were compared to BP, MF, CC GO types. GO terms significantly enriched in the unique ATAC-seq peaks ($p < 0.05$) and in DEGs ($p < 0.05$) were identified and stored independently as separate GO term lists for untreated and idling datasets.

Correlation Analysis: The $-\log_{10}$(p-value) was calculated for terms shared between the lists associated with the separate modalities, ranking terms based on statistical significance.

Spearman correlation was calculated between the significant GO terms using the *ggpubr* package (version 0.4.0) for each GO type.

Calcium flux assays

Data acquisition: SKMEL5 barcoded cells were plated onto a 384 well, tissue culture treated plate 24 hours before imaging at a density of 10,000 cells/well. For the treated condition, cells were treated with 8 µM PLX4720, a vemurafenib derivative, for 8 days with fresh media/drug swapped out every 3 days. Untreated control cells were taken from the same cell line culture which was maintained separately while the treatment condition was exposed to PLX4720, being split down when necessary to maintain healthy growth conditions. On the day of experimentation, the 384 well plate with all treated and untreated cells were incubated with 4 µM Fluo-8-AM in fresh culture media (10% FBS) for 1 hour at room temperature, as recommended by the manufacturer (AAT Bioquest). Dye containing media was removed and Hanks Buffered Saline Solution (HBSS, 10 mM HEPES, no Ca^{2+}) was used to wash the wells of excess dye, followed by removal and addition of 20 µL of fresh HBSS (no Ca^{2+}) for use as the assay buffer. The plate was loaded into a kinetic imaging instrument (Panoptic, by Waveguide Biosciences), which records the fluorescent intensity emitted by each well of the 384 well plate. A three-addition protocol was used to add the various drugs and assay conditions to the plate during the SOCE assay. Drug Addition plates were loaded with assay buffer (HBSS, with or without Ca^{2+}) and thoroughly mixed immediately before imaging. Add conditions were split into three parts: 1) Cyclopiazonic Acid (CPA; final concentration of 50 µM) to inhibit activity of Sarcoendoplasmic Reticulum Calcium ATPase (SERCA), leading ER Ca^{2+} release; 2) Addition of Ca^{2+} to the assay condition to activate SOCE activity; and 3) Addition of the Ca^{2+} ionophore, Ionomycin (final concentration of 5 µM), was used to generate maximal signal intensity to control for variations in cell count in individual wells (this was particularly important since drug treated idling cells experienced increased washout due to the stressful nature of sustained BRAF inhibition). Fluo-8-AM was excited with [480 nm] and imaged at [538 nm], with a frequency of 1 Hz. The CPA treatment condition was imaged for 260 seconds before addition of Ca^{2+}, followed by 270 seconds of imaging before addition of 5 µM Ionomycin. Treatment conditions were replicated in sets of 8 and average values traced with 95% confidence intervals.

Data analysis: Fluorescence data were normalized by dividing data from each well by the first fluorescence value at the start of the experiment. The ionomycin peak was used as a control for the number of cells in each treatment group, as the idling population tends to have less cell than the untreated population. Therefore, the mean ionomycin treatment peak was calculated for each treatment group (i.e., idling and untreated), and data from each treatment group were divided by the corresponding mean ionomycin peak value to account for the change in the number of cells in the assay. For comparison of calcium flux between the treatment groups, the lowest values were the zero starting point (on the y-axis) in the plot for each of the curves. A mean and 95% confidence interval were calculated for each time point and plotted using *ggplot*.

Ferroptosis-induction experiments

Plates of H2B-GFP-labeled SKMEL5 cells were treated with either vehicle (DMSO) or BRAFi (8μM PLX4720) for eight days incubated at 37°C and 5% CO_2, changing media (with vehicle/drug) every three days. BRAFi-treated cells were plated at ~2500 cells per well in a black, clear-bottom 96-well plate (Falcon). After cell seeding, RSL3, with or without Fer-1, was added the following morning, with media changes every three days (six replicates per condition). Plates were imaged using automated fluorescence microscopy (Cellavista Instrument, Synentec). Twenty-five non-overlapping fluorescent images (20X objective, 5x5 montage) were taken twice daily for a total of 150 hours or until confluency. Cellavista image segmentation software (Synentec) was utilized to calculate nuclear count (i.e., cell count) per well at each time point (Source = FITC, Dichro = FITC, Filter = FITC, Emission Time = 800μs, Gain = 20x, Quality = High, Binning = 2x2). Cell nuclei counts across wells were normalized to time of drug treatment and used to calculate a DIP rate (stable linear growth rate). A dose-response curve was calculated across replicates using the *drm* R package with a 4-parameter log-logistic function, with DIP rate as the drug effect. Replicates were used to calculate means and 95% confidence intervals for the dose-response curves. IC_{50} values were calculated for each condition and plotted as vertical dashed lines. Data was visualized using the ggplot2R package (version 3.2.0).

Model and Experimental Analysis Code Availability. The codes used to generate model simulations and analyze experimental data are publicly available via GitHub, or from the corresponding author upon request.

Data Availability. The sequencing datasets generated in this study can be found in the gene expression omnibus and sequence read archive. Additional experimental data will be available from the corresponding author upon request.

ACKNOWLEDGEMENTS

We thank Emily Hodges and Kelly Barnett for ATAC-seq reagents and experimental advice. We also thank Jing Hao for reagent acquisition and Tony Capra, Christian Meyer, Sarah Maddox Groves, Carlos Lopez, Alissa Weaver, John McLean, Bruce Damon, and Ken Lau for useful discussions.

Sequencing studies were performed by the Vanderbilt Technologies for Advanced Genomics (VANTAGE) core facility at Vanderbilt University Medical Center with help from Angela Jones, Karen Beeri, Jamie Roberson, Latha Raju, and Matthew Scholz. Cellular barcode library construction and transduction were performed in the Brock laboratory at The University of Texas at Austin. Data processing and model simulations were performed using resources at the Advanced Computing Center for Research and Education (ACCRE) at Vanderbilt University.

This work was supported by the following funding sources: C.E.H., National Institutes of Health (NIH) Ruth L. Kirschstein National Research Service Award (NRSA, F31-CA221147) and Chemical-Biology Interface Training Grant (T32-GM0650); L.A.H., National Cancer Institute (NCI) Transition

781 Career Development Award to Promote Diversity (K22-CA237857-01A1); D.R.T., NIH Research
782 Specialist Award (1R50CA243783); V.Q., NCI Emerging Questions in Cancer Systems Biology (U01
783 CA215845), NCI Research Centers for Cancer Systems Biology (U54 CA217450), NCI Predictive
784 Multiscale Models for Biomedical, Biological, Behavioral, Environmental and Clinical Research
785 (U01 CA174706), and Quantitative Systems Biology Center at Vanderbilt University.
786
787 COMPETING INTERESTS
788
789 The authors declare no competing interests.
790
791 AUTHOR CONTRIBUTIONS
792
793 Conceptualization, C.E.H., L.A.H., and V.Q.; Investigation and experiments, A.A., B.B.P., C.E.H.,
794 D.R.T., K.E.J., P.E.S.; Bioinformatic Analysis, B.B, C.E.H.; Modeling, C.E.H. and L.A.H.; Writing,
795 B.B., C.E.H. and V.Q.; Review and Editing, A.B., B.B., C.E.H., L.A.H., and V.Q.

REFERENCES

1. Liu J, Dang H, Wang XW. The significance of intertumor and intratumor heterogeneity in liver cancer. *Exp Mol Med* 2018; **50**: e416.
2. Inde Z, Dixon SJ. The impact of non-genetic heterogeneity on cancer cell death. *Crit Rev Biochem Mol Biol* 2018; **53**: 99–114.
3. Hayford CE, Tyson DR, Robbins CJ, Frick PL, Quaranta V, Harris LA. An in vitro model of tumor heterogeneity resolves genetic, epigenetic, and stochastic sources of cell state variability. *PLOS Biol* 2021; **19**: e3000797.
4. Huang S. Genetic and non-genetic instability in tumor progression: link between the fitness landscape and the epigenetic landscape of cancer cells. *Cancer Metastasis Rev* 2013; **32**: 423–448.
5. Brock A, Chang H, Huang S. Non-genetic heterogeneity--a mutation-independent driving force for the somatic evolution of tumours. *Nat Rev Genet* 2009; **10**: 336–42.
6. Pisco AO, Huang S. Non-genetic cancer cell plasticity and therapy-induced stemness in tumour relapse: 'What does not kill me strengthens me'. *Br J Cancer* 2015; **112**: 1725–1732.
7. Paudel BB, Harris LA, Hardeman KN, Abugable AA, Hayford CE, Tyson DR *et al.* A nonquiescent 'idling' population state in drug-treated, BRAF-mutated melanoma. *Biophys J* 2018; **114**: 1499–1511.
8. Aranda-Anzaldo A, Dent MAR. Landscaping the epigenetic landscape of cancer. *Prog Biophys Mol Biol* 2018; **140**: 155–174.
9. Sharma S V, Lee DY, Li B, Quinlan MP, Takahashi F, Maheswaran S *et al.* A chromatin-mediated reversible drug-tolerant state in cancer cell subpopulations. *Cell* 2010; **141**: 69–80.
10. Hata AN, Niederst MJ, Archibald HL, Gomez-Caraballo M, Siddiqui FM, Mulvey HE *et al.* Tumor cells can follow distinct evolutionary paths to become resistant to epidermal growth factor receptor inhibition. *Nat Med* 2016; **22**: 262–269.
11. Ramirez M, Rajaram S, Steininger RJ, Osipchuk D, Roth MA, Morinishi LS *et al.* Diverse drug-resistance mechanisms can emerge from drug-tolerant cancer persister cells. *Nat Commun* 2016; **7**: 10690.
12. Oren Y, Tsabar M, Cuoco MS, Amir-Zilberstein L, Cabanos HF, Hütter J-C *et al.* Cycling cancer persister cells arise from lineages with distinct programs. *Nat 2021 5967873* 2021; **596**: 576–582.
13. Jia D, Paudel BB, Hayford CE, Hardeman KN, Levine H, Onuchic JN *et al.* Drug-tolerant idling melanoma cells exhibit theory-predicted metabolic low-low phenotype. *Front Oncol* 2020; **10**: 1426.
14. Workman P, Travers J. Cancer: drug-tolerant insurgents. *Nature* 2010; **464**: 844–5.
15. Gutierrez C, Al'Khafaji AM, Brenner E, Johnson KE, Gohil SH, Lin Z *et al.* Multifunctional barcoding with ClonMapper enables high-resolution study of clonal dynamics during tumor evolution and treatment. *Nat Cancer 2021 27* 2021; **2**: 758–772.
16. Becht E, McInnes L, Healy J, Dutertre CA, Kwok IWH, Ng LG *et al.* Dimensionality reduction for visualizing single-cell data using UMAP. *Nat Biotechnol* 2019; **37**: 38–47.
17. Xie Y, Hou W, Song X, Yu Y, Huang J, Sun X *et al.* Ferroptosis: process and function. *Cell Death Differ* 2016; **23**: 369–379.

18 Boumahdi S, de Sauvage FJ. The great escape: tumour cell plasticity in resistance to targeted therapy. *Nat Rev Drug Discov 2019 191* 2019; **19**: 39–56.

19 Gupta PB, Pastushenko I, Skibinski A, Blanpain C, Kuperwasser C. Phenotypic plasticity: driver of cancer initiation, progression, and therapy resistance. *Cell Stem Cell* 2019; **24**: 65–78.

20 Rees M, Jessica C, Metcalf E, Childs DZ. Bet-hedging as an evolutionary game: the trade-off between egg size and number. *Proc Biol Sci* 2010; **277**: 1149–51.

21 Jolly MK, Kulkarni P, Weninger K, Orban J, Levine H. Phenotypic plasticity, bet-hedging, and androgen independence in prostate cancer: Role of non-genetic heterogeneity. Front. Oncol. 2018; **8**: 50.

22 Shaffer SM, Dunagin MC, Torborg SR, Torre EA, Emert B, Krepler C *et al.* Rare cell variability and drug-induced reprogramming as a mode of cancer drug resistance. *Nature* 2017; **546**: 431–435.

23 Emert BL, Cote CJ, Torre EA, Dardani IP, Jiang CL, Jain N *et al.* Variability within rare cell states enables multiple paths toward drug resistance. *Nat Biotechnol 2021 397* 2021; **39**: 865–876.

24 Gray JW, Mills GB. Large-Scale Drug Screens Support Precision Medicine. *Cancer Discov* 2015; **5**: 1130–2.

25 Huang S, Kauffman S. How to escape the cancer attractor: Rationale and limitations of multi-target drugs. *Semin Cancer Biol* 2013; **23**: 270–278.

26 Lee MJ, Ye AS, Gardino AK, Heijink AM, Sorger PK, MacBeath G *et al.* Sequential application of anticancer drugs enhances cell death by rewiring apoptotic signaling networks. *Cell* 2012; **149**: 780–94.

27 Hardeman KN, Peng C, Paudel BB, Meyer CT, Luong T, Tyson DR *et al.* Dependence on glycolysis sensitizes BRAF-mutated melanomas for increased response to targeted BRAF inhibition. *Sci Rep* 2017; **7**: 42604.

28 DeTomaso D, Jones MG, Subramaniam M, Ashuach T, Ye CJ, Yosef N. Functional interpretation of single cell similarity maps. *Nat Commun* 2019; **10**: 4376.

29 Love MI, Huber W, Anders S. Moderated estimation of fold change and dispersion for RNA-seq data with DESeq2. *Genome Biol* 2014; **15**: 1–21.

Figure 1

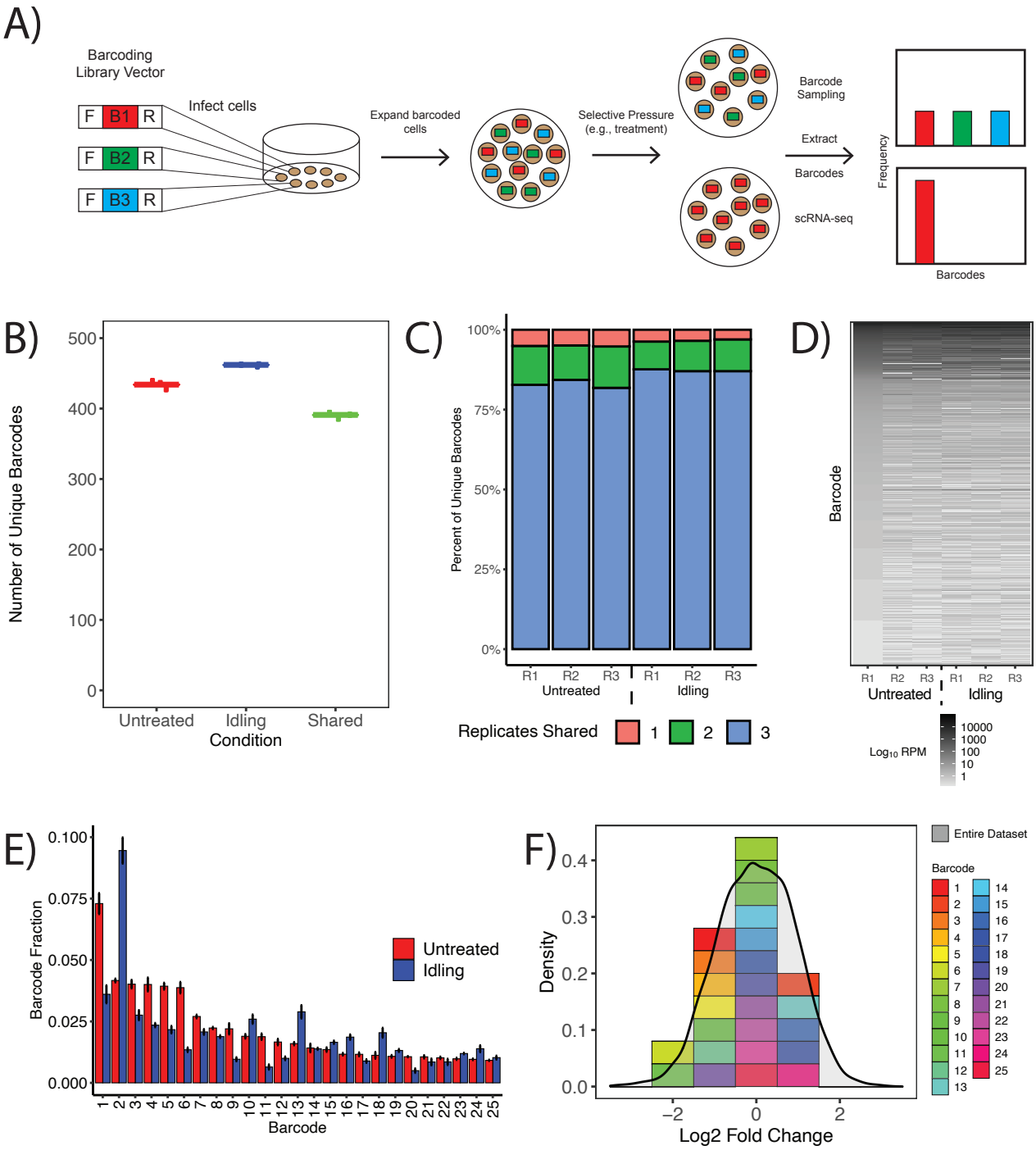

Figure 2

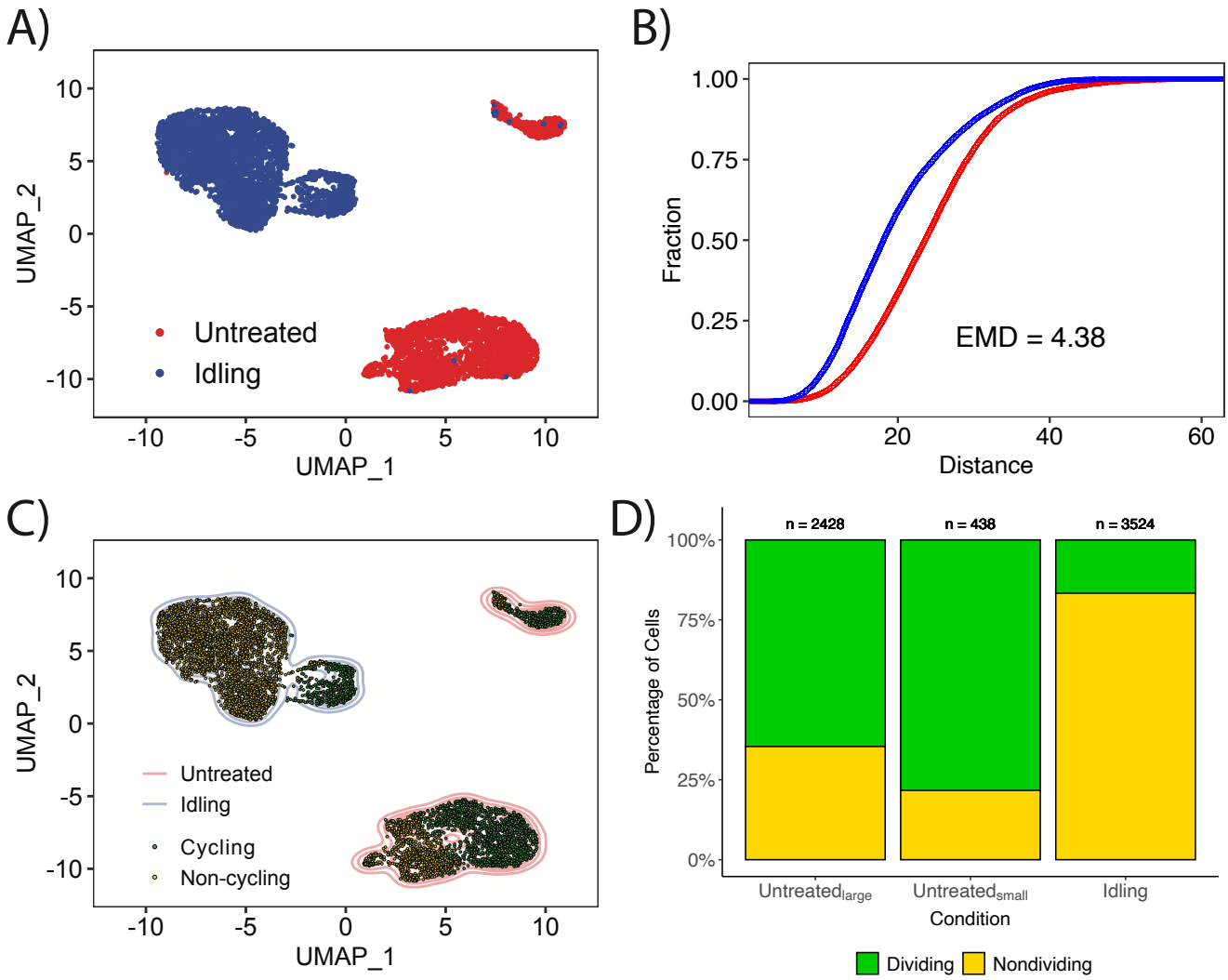

Figure 3

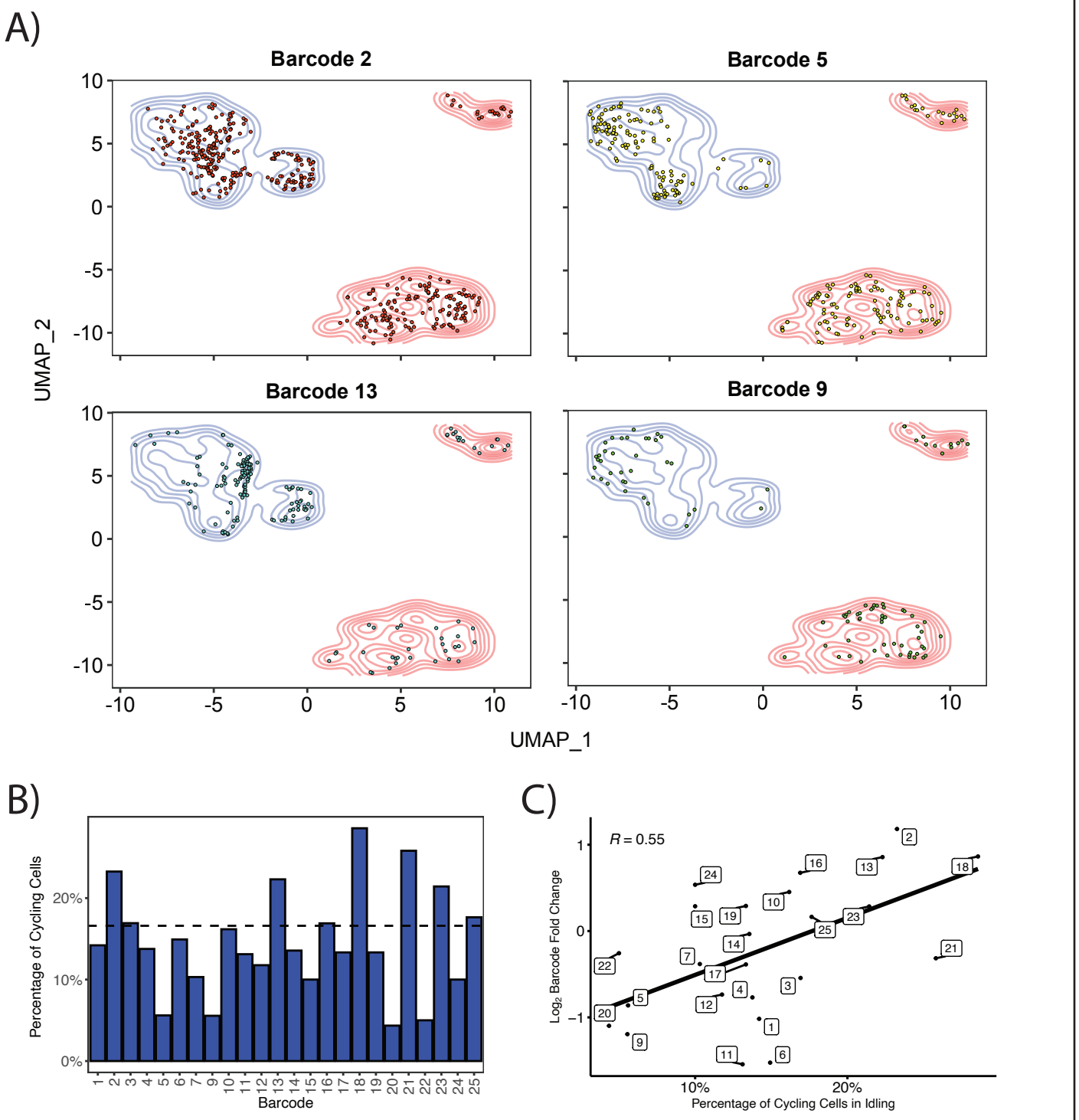

Figure 4

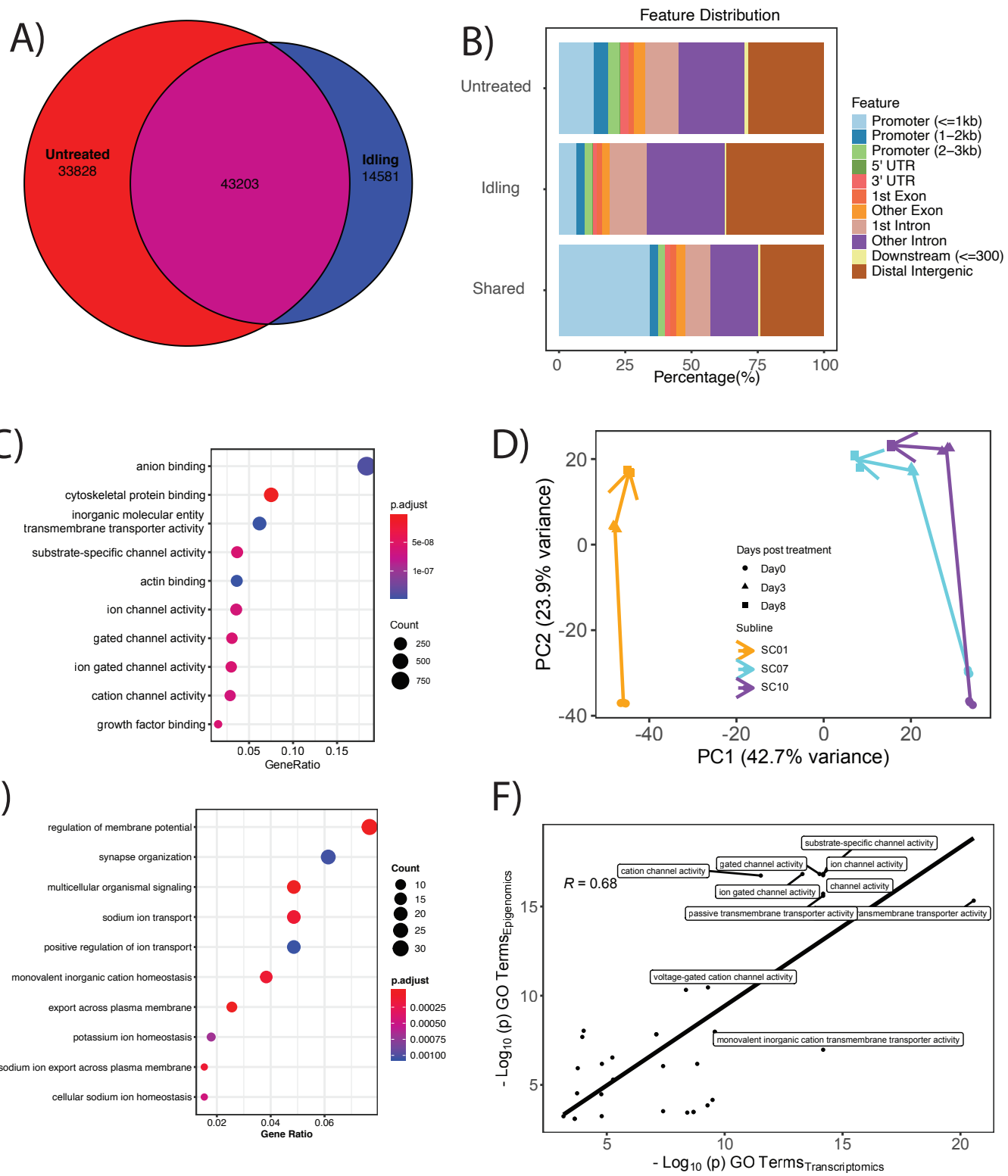

Figure 5

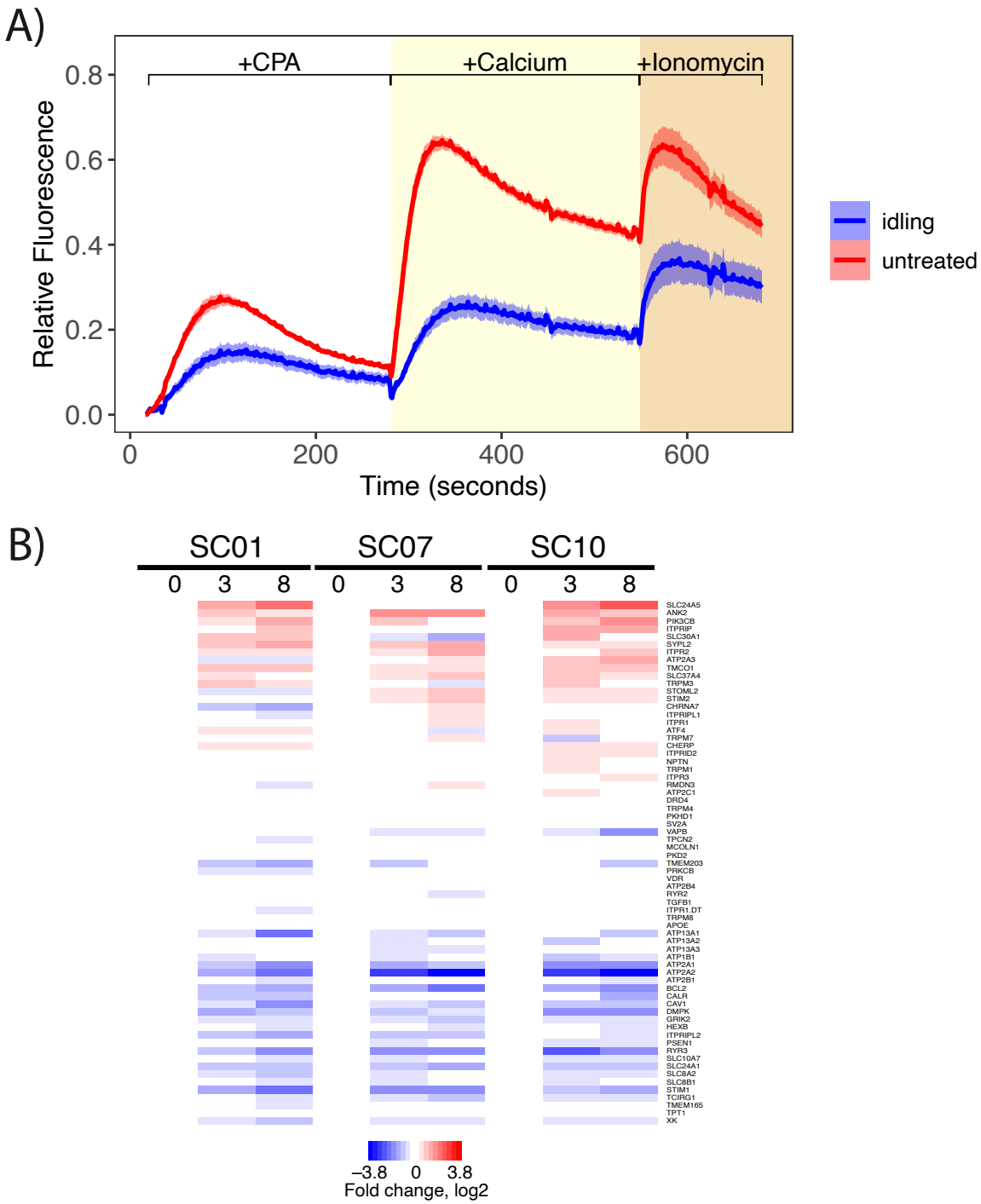

Figure 6